Available online at www.sciencedirect.com
SCIENCE DIRECT
International Journal of Multiphase Flow 32 (2006) 389–412
International Journal of Multiphase Flow
www.elsevier.com/locate/ijmulflow

A detailed experimental investigation of well-defined, turbulent evaporating spray jets of acetone

Yung-Cheng Chen *, Sten H. Stårner, Assaad R. Masri

School of Aerospace, Mechanical and Mechatronic Engineering, The University of Sydney, Sydney, NSW 2006, Australia

Received 23 December 2004; received in revised form 26 September 2005

Abstract

This paper aims at investigating the detailed structure of turbulent non-reacting dilute spray flows using advanced laser diagnostics. A simple spray jet nozzle is designed to produce a two-phase slender shear flow in a co-flowing air stream with well-defined boundary conditions. The carrier flow is made intentionally simple and easy to model so that the focus can be placed on the important aspects of droplet dispersion and evaporation, as well as turbulence–droplet interactions. Phase Doppler interferometry is employed to record droplet quantities, while planar laser-induced fluorescence imaging is applied separately to obtain acetone vapour data. Measurements are conducted for four acetone spray jets in air at several axial stations starting from the nozzle exit. The combined liquid and vapour mass fluxes of acetone integrated across the jet at downstream locations agree satisfactorily with the total mass flow rate of acetone injected.

The development of droplet rms velocity for the spray jets investigated is quite different in its radial and axial components. Variation in the radial rms velocity of droplets conditioned on different size-classes, v', is subject mainly to the response of droplets to turbulent fluctuations of the carrier flow and is characterized by the droplet relaxation time, t_d. Deviation of v' from that of the carrier phase occurs when the Stokes number becomes greater than approximately unity. For the size-classified axial rms velocity, u', the importance of the time scale for the rate of the incremental change of the axial mean velocity in the radial direction, t_m, has been identified. The droplet rms velocity ratio, u'/v', increases substantially as the time scale ratio t_d/t_m becomes greater than approximately 0.3, indicating strong anisotropy in droplet dispersion. A higher axial mean slip velocity is found for larger droplets that also intensifies their evaporation, and hence the bulk evaporation rate. Turbulence effects, however, are most effective in enhancing the evaporation of relatively small droplets that can follow closely the turbulent fluctuations of the gas flow.

PACS: 47.55.Kf; 47.27.Wg; 42.87.Bg

Keywords: Spray jets; Phase Doppler interferometry; Drop dispersion; Evaporation

* Corresponding author. Tel.: +61 2 9351 2272; fax: +61 2 9351 7060.
E-mail addresses: ycchen@mech.eng.usyd.edu.au, yc.chen@unsw.edu.au (Y.-C. Chen).

0301-9322/$ - see front matter © 2005 Published by Elsevier Ltd.
doi:10.1016/j.ijmultiphaseflow.2005.09.002

1. Introduction

Spray flows are common in many industrial applications ranging from spray dryers, fluidized reactors, to liquid-fuelled furnaces, and direct-injection and rocket engines. The physicochemical processes of sprays occurring in these systems are usually coupled between the dispersed droplets, turbulence, and chemical reactions involved. Such complicated interactions have made spray control and optimization a formidable and challenging task in practice. Although substantial progress has been made in the development of computational fluid dynamics (CFD) codes, the prediction capability is still limited by the empiricism in models for drop dispersion, evaporation, and combustion (Sirignano, 1993; Gouesbet and Berlemont, 1999). Validation of these submodels relies heavily on the availability of comprehensive measurements of well-characterized evaporating sprays (Solomon et al., 1985; McDonell and Samuelsen, 1993, 1995; Sommerfeld, 1998) and spray flames (Widmann and Presser, 2002). However, experimental data sets of this kind are mostly generated for air-assisted pressure-atomizing injectors. With these practical configurations, the initial plane often has to be set at a location downstream of the injector where reliable measurements of spray properties become available and the simulation of liquid ligaments breaking up into drops is avoided. A sophisticated turbulence model is also required to handle the complicated flow field for air-assisted atomization, which is not ideal for testing of the various spray dynamics models (Faeth, 1996).

In view of this complication, the main objective of the present work is set out to establish a model problem that is well defined for the investigation of turbulent reacting and non-reacting sprays. A spray jet nozzle is developed to produce a two-phase slender shear flow with the boundary conditions clearly specified. The spray is generated upstream by a nebulizer and advected by an air stream through the nozzle, at the exit of which the droplet distribution becomes fairly uniform and the access to optical and hardware probes is easy. The carrier flow field downstream of the nozzle exit is fluid-mechanically simple, and gradient models are known to work well. The spray jet thus produced is similar to a two-phase jet flow laden with either solid particles (Modarress et al., 1984; Fleckhaus et al., 1987; Mostafa et al., 1989; Hardalupas et al., 1989; Prevost et al., 1996) or liquid droplets (Hetsroni and Sokolov, 1971; Zuev et al., 1986; Ye and Richards, 1996; Kennedy and Moody, 1998; Balachandar, 1998; Ferrand et al., 2001, 2003). This configuration avoids modelling difficulties that are often encountered near the spray injector, such as high injection speed, flow recirculation, steep axial gradients, and dense spray effects. Another objective of the spray nozzle developed here is to extend previous work on piloted turbulent jet diffusion flames (Bilger, 1992) into spray combustion. The combusting version of the current nozzle utilizes an annular premixed pilot flame on the thin burner lip to anchor the spray jet flames. Characteristics of such spray flames have been recently reported by Chen et al. (2002).

A two-phase spray jet possesses the essential complexities of droplet/turbulence interactions. The two-way coupling between the dispersed and the carrier phases (Berlemont et al., 1995) is further complicated by the presence of drop evaporation. Turbulent evaporating spray jets are therefore chosen for investigation in this work and the focus is placed on issues pertaining to droplet dispersion and evaporation. With well-specified boundary conditions, this configuration should serve as an appropriate scenario to examine the various models of drop dynamics incorporating the influences of turbulence on spray vaporization. Evaporating jets (Fan et al., 2001) or sprays (Bellan, 2000) encountered in practical applications often have a higher environmental temperature than the boiling temperature of the injected liquid. In this work liquid acetone is injected into air at ambient temperature. The saturated vapour pressure of acetone at 20 °C is 0.246 bar, approximately 10 times higher than that for water. This feature proves to be advantageous in that preheating of the carrier air flow is not needed for acetone spray jets to develop substantial evaporation. The use of acetone also enables the complementary laser-induced fluorescence measurements to be made such that the complete fuel concentration distributions can be obtained in both vapour and liquid phases to deduce the bulk evaporation rate with confidence.

In the following, the experimental set-up for laser diagnostics is first described, including the spray nozzle design and operating conditions of the spray jets investigated. The detailed initial conditions, which are essential to CFD computations, are reported on the nozzle exit plane. These include radial profiles of the droplet mean and root-mean-square (rms) velocities, the droplet mean diameters, and the mean acetone vapour concentration. Radial profiles of the droplet mean and rms velocities conditioned on different size classes are then presented at several downstream axial locations. These data should be useful for comparison with

model predictions. Typical scatter plots of the droplet velocity versus diameter are shown to illustrate the various aspects of turbulent drop dispersion. The radial spread rates for droplets at different size classes are derived to highlight their relative dispersion ability. Furthermore, the possibility of a self-similar velocity field is analyzed for the carrier flow and the droplets. Radial profiles of the Sauter mean diameters and those of the droplet and vapour mass fluxes are also reported at several axial locations. Effects of turbulence on droplet evaporation rate are discussed in the light of the size-classified number density distribution. Finally, the axial evolution of the area-integrated droplet mass flux across the jet is compared between the spray jets investigated, along with the bulk evaporation rate.

2. Experimental

2.1. Spray nozzle and test conditions

Fig. 1 shows a schematic diagram of the spray nozzle, which is externally tapered and centred on the exit plane of a wind tunnel. The tunnel has a dimension of 15 cm by 15 cm and supplies a filtered co-flowing air stream through a screen to avoid ambient disturbances and to provide a definite lateral boundary condition for modelling purpose. This co-flow has a uniform mean velocity, $\overline{U}_\infty$, of 3 m/s with less than 2% relative turbulence intensity. The co-flow turbulence is so low that it makes no significant addition to the jet turbulence. The nozzle is 75 mm long with an inner diameter, D, of 9.8 mm. Pressurized liquid acetone is fed into a glass concentric nebulizer which is placed upstream on the nozzle axis. No back-flow of liquid is detected at the bottom of the nozzle for all the test conditions. The flow rates of acetone and carrier air are regulated by rotameters to within 3% accuracy.

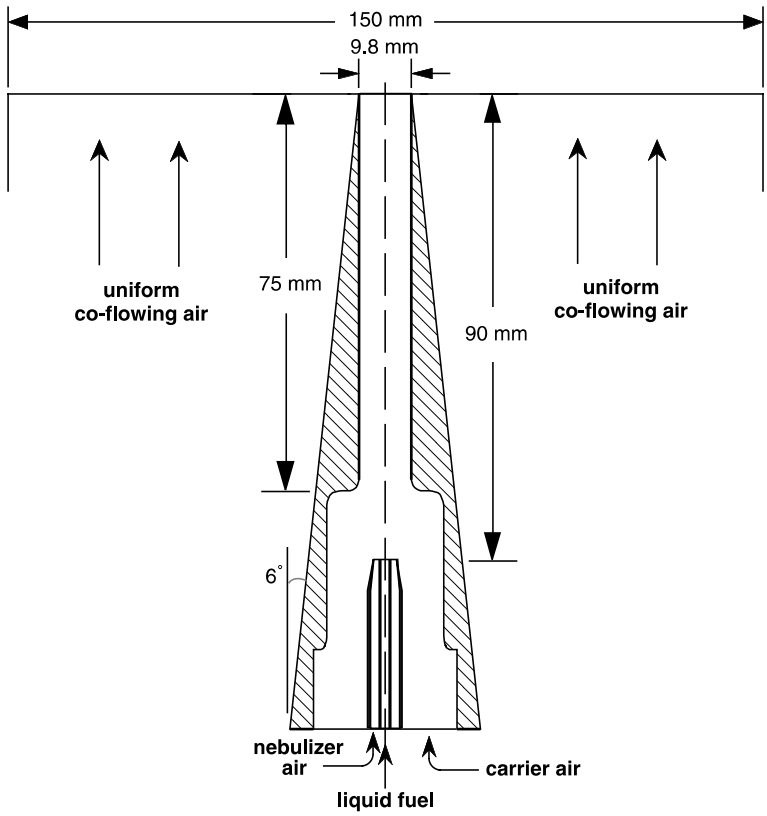

Fig. 1. Configuration of the spray jet nozzle.

Table 1
Experimental conditions of non-reacting spray jets. $\mu_g = 1.847 \times 10^{-4}$ g/cm s is the viscosity of ambient air

Spray jets	LFS	HFS	HFD	HCS
Carrier air flow rate, $\dot{M}$ (g/min)	135	270	270	270
Jet Reynolds number, $4\dot{M}/\pi D\mu_g$	15,800	31,600	31,600	31,600
Liquid fuel injection rate, $\dot{G}$ (g/min)	7.0	7.0	11.7	7.0
Integrated vapour flux at nozzle exit (g/min)	5.9	4.0	6.2	2.5
d_{32} at nozzle exit (μm)	13.7	18.1	17.5	23.9
Gas temperature at nozzle exit, T (°C)	2	17	13	20

Four acetone spray jets are investigated, and their operating conditions are listed in Table 1. The flow rate of carrier air is adjusted for either low (L) or high (H) speed at a jet Reynolds number of 15,800 or 31,600, respectively. The mass flow rate of acetone injected into the nebulizer, $\dot{G}$, varies between sparse (S), 7.0 g/min, and dense (D), 11.7 g/min, loadings. Actually, all the spray jets studied here are sufficiently diluted as the ratio of the volumetric flow rate of the droplets to that of the air ranges from only 0.4×10^{-5} to 3.1×10^{-5} at the nozzle exit. Droplet–droplet interactions therefore can be safely assumed negligible. A fine (F) or coarse (C) droplet size distribution is achieved by controlling the pressure of nebulizer air at a mass flow rate less than 1% of that of the carrier air. The higher the nebulizer air pressure, the finer the droplet size distribution, and the smaller the Sauter mean diameter, d_{32}, at nozzle exit. The mean droplet size at nozzle exit is also affected by continuous evaporation of droplets travelling in the nozzle. A low-speed jet flow has a longer spray residence time for droplet evaporation to occur in the nozzle. Hence, as shown in Table 1, the value of d_{32} at nozzle exit is smaller for LFS than for the high-speed spray jets of HFS and HFD, all having the same nebulizer air pressure.

2.2. Phase Doppler interferometry (PDI)

Droplet diameter, d, the axial, x-, and radial, r-, components of droplet velocity, U and V, droplet number density, N, and its volume flux are measured with a two-component phase Doppler interferometer in this work. The PDI instrument is arranged in the forward scattering mode. Parameter settings of the receiver and in the data-acquisition software are listed in Table 2. An Ar^+-laser is coupled to the transmitter via a fiber optic assembly. At the measurement volume, the power for each beam is 50–100 mW and the fringe spacing is 3 μm with a beam waist of approximately 110 μm. The inherent phase difference between the dual Photomultiplier (PMT) detectors has been pre-calibrated depending on the applied voltage and the data sampling frequency, which are also changed at some measurement locations.

Software coincidence has been imposed on velocity measurements together with the intensity validation scheme applied to drop size measurements. The software built-in probe volume correction (PVC) is also implemented to compensate for the fact that smaller droplets are detected over a smaller region in the probe volume. The PVC option was transit time method, analytical factor 2. The reported droplet mean diameters, d_{ij}, are corrected for the different probe volume width as

Table 2
Parameters of the PDI instrument

Focal length of the receiving lens	300 mm
Slit aperture	100 μm
Collection off-axis angle	45°
PMT high voltage	350–400 V
Sampling rate	40–80 MHz
Low pass filter	10 MHz
Mixer frequency	36 MHz
Diameter range	1.6–80 μm

$$d_{ij} = \left(\frac{\sum_{k=1}^{n} g_k d_k^i}{\sum_{k=1}^{n} g_k d_k^j} \right)^{\frac{1}{(i-j)}} \quad \text{for } i \neq j \tag{1}$$

where n is the number of size bins used for the PDI measurements and g_k is the probe-volume corrected particle count of the kth bin.

PDI measurements are scanned across the spray jet at the normalized axial locations of $x/D = 0.5$, 5, 10, 15, 20, and 25 downstream of the nozzle exit plane. As drop dispersion is highly size-dependent, the reported droplet mean and rms velocities are conditioned on different size classes for comparison with model predictions based on the Lagrangian formulation. It is well known (McLaughlin and Tiederman, 1973) that the measured ensemble averages do not represent the true time averages, which may be obtained by employing the correction method of the interarrival time weighting. The relative difference, however, is found to be less than 0.2% on the axis and approximately 3% on the edge of the spray jet for the axial mean velocity, $\overline{U}$, and of the order of 2% across the jet for the axial and radial rms velocities, u' and v'.

The refractive index of acetone increases by approximately 0.00056 ± 0.00001 for every 1 °C decrease. This temperature dependency may potentially influence the droplet sizing measurements for the optical configuration used. For an estimated maximum temperature variation of 20 °C in this work, the refractive index of acetone droplets increases from 1.3588 at 20 °C to 1.3700 at 0 °C. The corresponding slope value of the phase/size curve is calculated to be 0.6347 at 20 °C and 0.6307 at 0 °C for a collection angle of 45°. Such a difference has a negligible effect on the droplet diameter measured, as a fixed slope value of 0.63 was used for data acquisition.

Random errors of the droplet mean and rms velocities as well as its mean diameters are given in Table 3 based on scattering of five data sets of ten separate measurements at the same location on the nozzle exit plane. The different sets of measurements are taken in a time frame of approximately 2 weeks during which all the data reported in this paper are collected. During the experimental campaign consistent data have been obtained for each of the test conditions at different time, indicating that the spray jets were all in a steady state while measurements were taken.

2.3. Laser-induced acetone fluorescence

PDI measurements of the droplet mass flux are notoriously difficult and unreliable unless an accurate calibration of the probe volume size is made (McDonell and Samuelsen, 1996; Widmann et al., 2001). To enable a check on the performance of the PDI instrument, acetone vapour concentration in the spray jets investigated is measured independently with planar laser-induced fluorescence (PLIF). LIF images of the acetone spray, including both vapour and droplets, are produced by forming a 6 mm-high sheet from the 266 nm quadrupled output of a pulsed Nd:YAG laser, and are captured at 90° to the sheet plane. The incident UV beam intensity has been monitored by a power meter to be within 5% before and after the measurements. An unintensified 12-bit CCD camera is used to maximize resolution and dynamic range. Each pixel represents 18.8 μm in the image plane. The camera lens is opaque to UV radiation, so that only the broadband fluorescence in the visible range is recorded.

The LIF signal in the gas phase is proportional to the number density of acetone vapour (Bryant et al., 2000). Quantitative calibration is made by imaging a vapour/air mixture of constant composition produced

Table 3
Experimental uncertainty

Variable	Uncertainty (%)
Axial mean velocity, $\overline{U}$	0.2
Axial and radial rms velocity, u' and v'	3
Sauter mean diameter, d_{32}	4
Mean vapour concentration, $\overline{X}_{ac}$	2
Vapour mass flux, $\dot{m}_g$	4
Droplet mass flux, $\dot{m}_d$	10

by bubbling air through an acetone liquid reservoir. The acetone number density in this calibration mixture is determined by Rayleigh scattering, relative to air. Beam attenuation, quenching, and fluorescence trapping are found to be insignificant in this dilute flow.

However, the extraction of vapour data only from the imaging measurements would require removal of the LIF trace of the droplets. The droplet LIF signature is sharp-edged, and typically less than 20% of the imaging area is occupied by droplets. Thus, they are easily identified by their high gradients and are removed by digital filtering. The 'holes' left are filled by the average of the immediate surroundings. Fig. 2 shows the comparison of an instantaneous LIF-acetone image before and after the removal of the droplets. There are two potential sources of error in this approach. First, optical wakes behind the droplets must exist and have been studied by Bazile and Stepowski (1995). Such wakes would reduce the vapour fluorescence intensity. However, they are completely undetectable in the sprays investigated here, most likely due to our use of a high-energy laser beam and an incident wavelength of much lower fluorescence yield than that by Bazile and Stepowski (1995). Second, droplets below 3 μm may go undetected, as indicated by a comparison of number density in the images with the PDI data. However, these droplets contain less than 1% of the total droplet mass, and so do not contribute significantly by being double-counted in the overall acetone flux, assuming they are also counted in the PDI data.

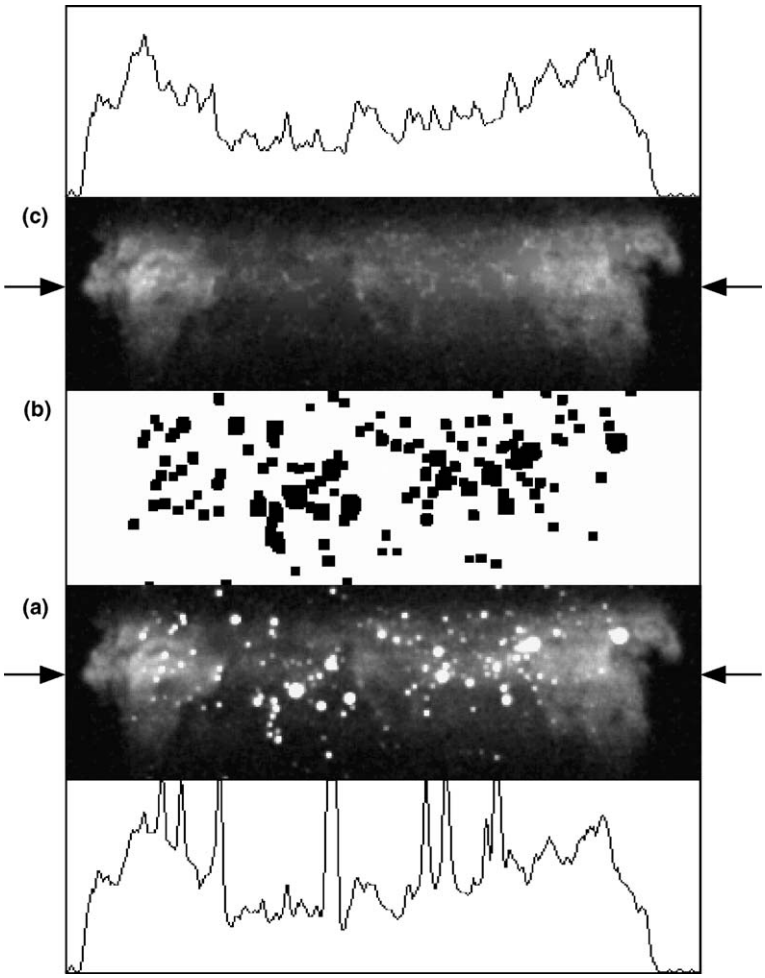

Fig. 2. (a) An instantaneous LIF-acetone image; (b) the identification of droplet positions; and (c) the corrected LIF-acetone image. Also shown is the corresponding line scan taken at the position indicated by the arrows on the images before and after the droplet removal. The image size is 12.95 mm wide and 3.95 mm high.

At each axial location where PDI measurements are made, 30 instantaneous LIF images are collected to derive the radial profile of the mean acetone vapour molar concentration, $\bar{c}_{ac,g}$. It is found that $\bar{c}_{ac,g}$ is quite insensitive to the threshold level chosen for droplet detection and removal; this is because the fraction of the image involved is small, and the loss of excess vapour around each droplet is partly compensated for by replacing the droplet area itself by vapour. The resulting error in $\bar{c}_{ac,g}$ from this source is estimated to be below 2%.

The steady-state mass flux of acetone vapour in the axial direction, $\dot{m}_g$, is then calculated as

$$\dot{m}_g = \bar{c}_{ac,g} W \overline{U}|_{d<3\,\mu m} \tag{2}$$

where W is the molecular weight of acetone. The neglect of turbulent fluxes in Eq. (2) is estimated, following Antonia et al. (1975), to reduce $\dot{m}_g$ by 2–4%. Also, the axial mean velocity of droplets conditioned on diameters less than 3 μm, $\overline{U}|_{d<3\,\mu m}$, is assumed here to be the same as the axial mean velocity of the gas flow. This is considered a reasonable approximation for the present work as it will be shown later that the Stokes number for these small droplets is much less than unity.

The mean acetone vapour mole fraction, $\overline{X}_{ac}$, is also derived as

$$\overline{X}_{ac} = \bar{c}_{ac,g} \frac{RT}{P}, \tag{3}$$

where R is the universal gas constant. The temperature of the carrier air, T, at the nozzle exit plane decreases due to upstream droplet evaporation in the nozzle. Based on energy conservation, the value of T can be below the ambient temperature of 25 ± 1 °C by 8 °C for spray jet HFS and by 23 °C for spray jet LFS, as shown in Table 1.

3. Results and discussion

3.1. Initial conditions

A particular feature of the spray jets investigated in this work is that the droplet initial conditions are homogeneous in the core region and that the flow field is free from complications such as recirculation or swirl. This is shown in Fig. 3 by the radial profiles of droplet velocity averages at the normalized axial location of $x/D = 0.5$ for the high- and low-speed spray jets, HFS and LFS. The distributions of the axial mean velocity, $\overline{U}$, and the axial and radial rms velocities, u' and v', are relatively uniform for droplets conditioned on different size classes. The initial droplet velocity profiles are also quite similar for the three high-speed spray jets (not shown), particularly in the velocity averages conditioned on droplets smaller than 3 μm. Flow modification effects in the nozzle tube therefore can be neglected for the range of mass loadings and nebulizer droplet size distributions varied here.

Distinct droplet dispersion effects, on the other hand, are clearly observed in Fig. 3: the droplet diameter and its axial velocity are negatively correlated in the core region at the nozzle exit, except close to the nozzle edge where the correlation becomes positive. The predominant negative correlation indicates that large droplets do not follow the axial gas flow development along the nozzle as readily as the small ones. Droplets initially released from the nebulizer are travelling more slowly than the carrier air with a negative mean axial slip velocity, $\overline{U}_s$, defined as

$$\overline{U}_s = \overline{U} - \overline{U}|_{d<3\,\mu m} \tag{4}$$

where both $\overline{U}_s$ and $\overline{U}$ are size-classified mean velocities. Most droplets therefore are subject to the accelerating drag force while the developing air flow also increases its axial velocity in the nozzle core region. The droplet mean axial velocity can be described by the equation:

$$t_d \frac{d\overline{U}}{dt} = |\overline{U}_s| - t_d g \left(1 - \frac{\rho_g}{\rho_\ell}\right) \tag{5}$$

with the relaxation time t_d (the time it takes for a droplet to reach its terminal velocity) given as

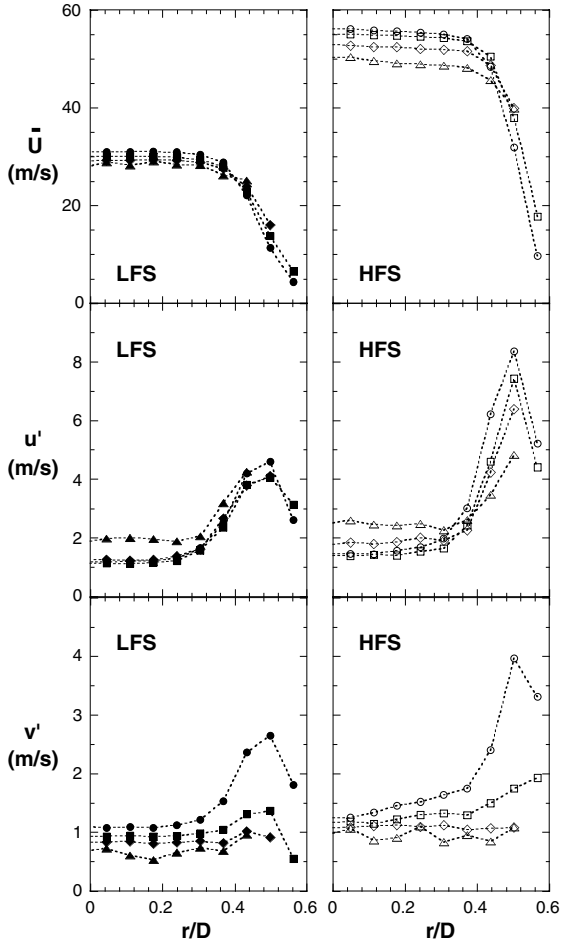

Fig. 3. Radial profiles of the axial mean velocity, $\overline{U}$, and the axial and radial rms velocities, u' and v', of droplets conditioned on different size classes ($d < 5$ μm: ○ and ●; 10 μm $< d <$ 20 μm: □ and ■; 20 μm $< d <$ 30 μm: ◇ and ◆; 30 μm $< d <$ 40 μm: △ and ▲) for spray jets LFS and HFS at $x/D = 0.5$.

$$t_{\mathrm{d}} = \frac{\rho_{\ell}}{\rho_{\mathrm{g}}} \frac{4d}{3C_{\mathrm{D}}|\overline{U}_{\mathrm{s}}|} \tag{6}$$

for droplets of diameter d. Here ρ is density and C_{D} is the drag coefficient. Subscripts 'ℓ' and 'g' stand for the droplet and gas properties, respectively. Small droplets have large drag coefficients and small t_{d} values. Hence, the droplet acceleration in Eq. (5) is greater for smaller droplets leading to higher $\overline{U}$ (and lower $|\overline{U}_{\mathrm{s}}|$) values at the nozzle exit. Fig. 3 also indicates that for a given droplet size class $|\overline{U}_{\mathrm{s}}|$ is greater in the high-speed than in the low-speed sprays on the exit plane. This is expected as less time is available for droplet acceleration when the spray jet has a higher axial mean velocity upstream of the nozzle exit. Although substantial spray evaporation occurs in the nozzle tube, detailed analysis of Eq. (5) shows no obvious change in the dependency of $\overline{U}_{\mathrm{s}}$ on droplet diameter at the nozzle exit, assuming constant $\overline{U}|_{d<3\,\mu\mathrm{m}}$, a drag coefficient of $24/Re_{\mathrm{d}}$, and the d-square law for the decrease of droplet diameter. The weak effect of spray evaporation on droplet dispersion in the nozzle tube is also confirmed by Nijdam et al. (2004) from measurements in acetone and turpentine sprays. The relatively high boiling temperature of turpentine makes it almost non-volatile at ambient conditions.

It is also found on the nozzle exit plane that the rms fluctuations of both the axial and radial velocities are reduced as droplet diameter increases. This feature is attributed to the inertia effect since large droplets tend to maintain their speed and are less likely to respond to flow turbulence fluctuations. The size-classified radial

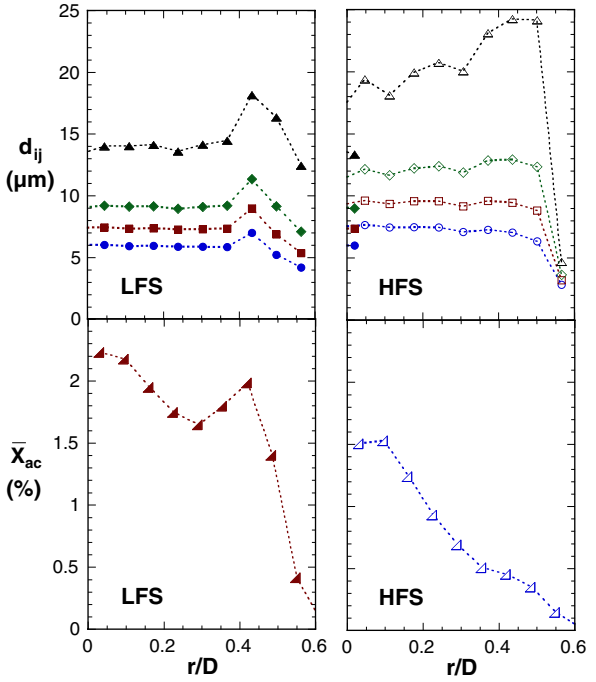

Fig. 4. Radial profiles of the various droplet mean diameters, d_{ij}, (d_{10}: ○ and ●; d_{20}: □ and ■; d_{30}: ◊ and ♦; d_{32}: △ and ▲) and the mean acetone vapour mole fraction, $\overline{X}_{ac}$, for spray jets LFS and HFS at $x/D = 0.5$.

rms velocity, v', therefore decreases with increasing droplet diameter of the size class, particularly on the nozzle edge where shear-layer turbulence develops as shown in Fig. 3. A similar size class dependency, however, is not evident for the axial rms velocity, u'. Instead, higher values of u' are associated with the size-class of larger droplets near the jet centreline for the high-speed spray jet HFS. This spurious feature is caused by the strong non-linear dependency of $\overline{U}_s$ on droplet diameter compounded by the artificial size classification within a finite diameter range.

Radial profiles of the various droplet mean diameters, d_{ij}, measured at $x/D = 0.5$ and the initial distribution of the mean acetone vapour mole fraction, $\overline{X}_{ac}$, are plotted in Fig. 4 for both spray jets HFS and LFS. A decreasing value of d_{10} is found with increasing radius for spray jet HFS, indicating a gradually finer droplet distribution towards the nozzle edge. The Sauter mean diameter, d_{32}, on the other hand increases, in line with an increase of the volume-averaged diameter, d_{30}, and a slight decrease of the surface-averaged diameter, d_{20}. All these droplet mean diameters decrease drastically for $r/D > 0.5$. Similar qualitative features of d_{ij} are also observed for the other two high-speed spray jets investigated here. For the low-speed spray jet LFS, the magnitudes of d_{ij} remain relatively constant across the nozzle exit. Towards the nozzle edge, all the droplet mean diameters increase slightly and then decrease drastically further outwards. The local peaks of d_{ij} at $r/D \approx 0.4$ for LFS coincide with a local maximum of $\overline{X}_{ac}$ as shown in Fig. 4. During the experiment, liquid acetone was observed attaching to the inner wall of the nozzle and generating large droplets and locally high acetone vapour concentration at the nozzle exit. For all the spray jets investigated here, the maximum of $\overline{X}_{ac}$ is still below the saturated value, such that the fluctuation of local acetone vapour concentration has little effect on droplet evaporation.

3.2. Analysis of self-similar droplet velocity field

Radial profiles of the axial mean and rms velocities conditioned on droplets of different size classes are plotted in Fig. 5 at several axial locations from $x/D = 5$ to 25 for spray jet LFS. Those for the high-speed spray jets (Chen et al., 2001) show qualitatively the same trend. The non-reacting spray jet LFS complements the spray

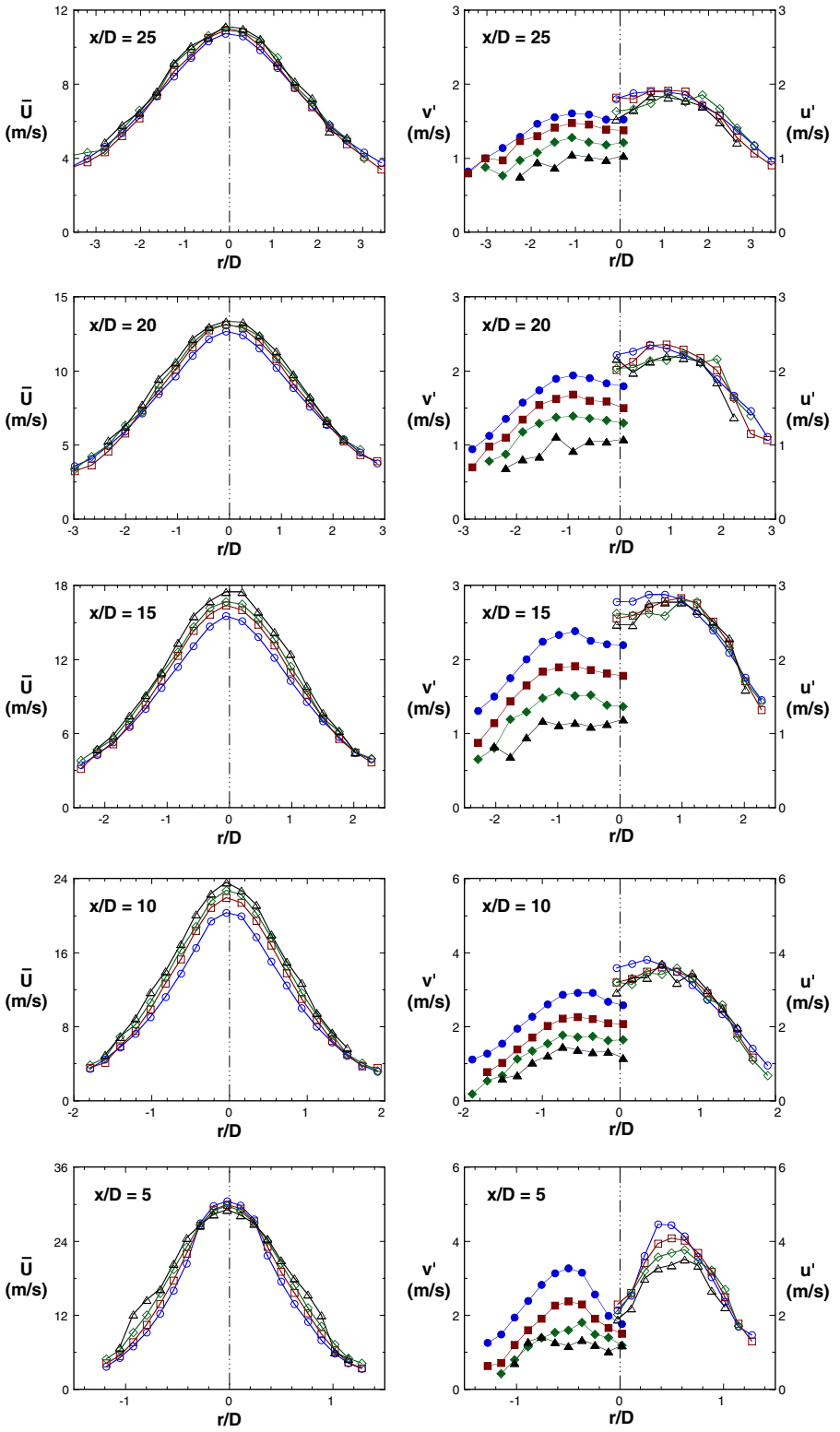

Fig. 5. Radial profiles of the axial mean velocity, $\overline{U}$, and the axial and radial rms velocities, u' and v', of droplets conditioned on different size classes ($d < 5$ μm: ○ and ●; 10 μm $< d <$ 20 μm: □ and ■; 20 μm $< d <$ 30 μm: ◊ and ♦; 30 μm $< d <$ 40 μm: △ and ▲) for spray jet LFS.

jet flame AHF reported by Chen et al. (2002) to form a comprehensive data set, which can be used for model validation of spray dynamics in CFD calculations.

The overall droplet velocity field shown in Fig. 5 indicates that the investigated spray behaves like a conventional jet flow. The axial mean velocity, $\overline{U}$, decreases along the jet centreline for all the droplet size classes and the spray jet diverges with increasing axial distance. Both the axial and radial rms velocities, u' and v', peak locally at approximately the same radial position and the peak location moves outwards as the spray jet diverges.

The normalized centreline axial mean, $\overline{U}_{CL}$, and rms, u'_{CL}, velocities for droplets of different size classes are shown in Fig. 6. The normalization is made by the centreline axial mean velocity measured at $x/D = 0.5$, $\overline{U}_0$, and the co-flow velocity, $\overline{U}_\infty$. Note that $\overline{U}_0$ is also conditioned on the corresponding size-class to keep the normalized mean value unity for all the size classes at $x/D = 0.5$. The mean velocity $\overline{U}_{CL}$ starts to decrease at the end of the potential core near $x/D = 5$. Beyond $x/D = 15$, the decay of the velocity excess, $\overline{U}_{CL} - \overline{U}_\infty$, conditioned on a particular size-class appears to follow the self-preserving relationship for a large-excess co-flowing jet flow (Hussein et al., 1994; Nickels and Perry, 1996):

$$\frac{\overline{U}_0 - \overline{U}_\infty}{\overline{U}_{CL} - \overline{U}_\infty} = \frac{1}{a}\left(\frac{x - x_0}{D}\right) \tag{7}$$

where a is a constant related to the decay rate of $(\overline{U}_{CL} - \overline{U}_\infty)/(\overline{U}_0 - \overline{U}_\infty)$, and x_0 represents the virtual origin. The curve-fitted value of a varies between 7.2 and 7.5 for droplets of different size classes, with slightly less deceleration for $(\overline{U}_{CL} - \overline{U}_\infty)/(\overline{U}_0 - \overline{U}_\infty)$ conditioned on larger droplets. This feature is consistent with previous observations made by Prevost et al. (1996) and de Vega et al. (2000) in non-evaporating sprays as the velocity decay is retarded for large droplets with significant inertia. The virtual origin, on the other hand, increases consistently from $-2.0D$ for $d < 3$ μm to $2.2D$ for 30 μm $< d <$ 40 μm. The increase of the virtual origin value with droplet size is most likely due to the present initial condition that large droplets are still accelerated within the potential core, and thus the incipient axial location of the centreline velocity decay is delayed. The normalized axial rms velocity, $u'_{CL}/\overline{U}_0$, appears to fall into the same distribution for droplets of different size classes in Fig. 6. This fortuitous feature is attributed to the marginal difference in the a values between droplets of different size classes and close to zero virtual origins for the spray jets investigated. The absolute magnitude of u'_{CL} increases rapidly downstream of the nozzle exit for all the size classes, and reaches the maximum value at approximately $x/D = 10$.

The slightly smaller decay rate of the normalized centreline axial mean velocity, $(\overline{U}_{CL} - \overline{U}_\infty)/(\overline{U}_0 - \overline{U}_\infty)$, for larger droplets is consistent with a relatively smaller expansion rate defined as $dr_{0.5}/dx$. $r_{0.5}$ is the radius at which the excess axial mean velocity, $\overline{U} - \overline{U}_\infty$, is half of the excess axial mean velocity on the centreline, $\overline{U}_{CL} - \overline{U}_\infty$. This is illustrated in Fig. 7 for spray jet LFS for which the normalized half-radius, $r_{0.5}/D$, increases

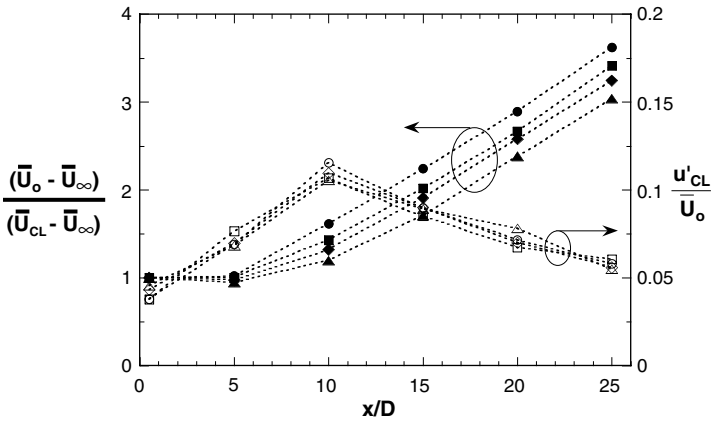

Fig. 6. Variation of the reciprocal of the normalized centreline axial mean velocity, $(\overline{U}_0 - \overline{U}_\infty)/(\overline{U}_{CL} - \overline{U}_\infty)$, and the normalized centreline axial rms velocity, $u'_{CL}/\overline{U}_0$, of droplets conditioned on different size classes ($d < 5$ μm: ○ and ●; 10 μm $< d <$ 20 μm: □ and ■; 20 μm $< d <$ 30 μm: ◇ and ◆; 30 μm $< d <$ 40 μm: △ and ▲) for spray jet LFS.

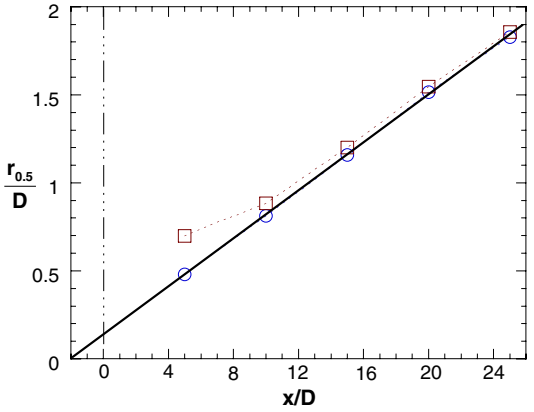

Fig. 7. Normalized half-radius, $r_{0.5}/D$, of the droplet axial mean velocity excess conditioned on $d < 3$ μm (○) and 30 μm $< d <$ 40 μm (□) for spray jet LFS. The solid line is the linear, least-squares fit.

linearly with the normalized axial distance, x/D, after $x/D = 10$ for both 'small' and 'big' droplets conditioned on $d < 3$ μm as well as in the range of 30 μm $< d <$ 40 μm, respectively. The exceptionally large $r_{0.5}$ at $x/D = 5$ for 'big' droplets with substantial inertia is caused by the particular initial condition here that these droplets are still accelerated by the carrier flow within the potential core. It appears therefore that the initial dispersion of larger droplets is stronger. As a result, the absolute value of $r_{0.5}$ is larger for bigger droplets along the axis, but gradually converges to the same for droplets of all size classes as can be inferred from the mean velocity profiles in Fig. 5. The downstream expansion rate derived from linear regression of the data in Fig. 7 is 0.068 for $d < 3$ μm and 0.065 for 30 μm $< d <$ 40 μm. The decreasing expansion rate with droplet size implies a relatively smaller radial dispersion for larger droplets at downstream locations. As there is no apparent mean slip velocity in the radial direction, the relative difference in the expansion rate is most likely caused by variations of turbulent transport in the radial direction between droplets of different diameters.

Fig. 7 also shows that the linear fit for small droplets of $d < 3$ μm intersects the horizontal axis, x/D, at the same value as the virtual origin derived from Fig. 6 using Eq. (7). The coincidence is consistent with the possible self-preserving feature of the underlying carrier flow field. To examine this feature, the normalized radial profiles of the axial mean velocity excess, $(\overline{U} - \overline{U}_\infty)/(\overline{U}_{CL} - \overline{U}_\infty)$, and the axial rms velocity, $u'/(\overline{U}_{CL} - \overline{U}_\infty)$, are plotted in Fig. 8 against $\zeta \equiv r/(x - x_0)$ for droplets conditioned on $d < 3$ μm. Experimental data of $(\overline{U} - \overline{U}_\infty)/(\overline{U}_{CL} - \overline{U}_\infty)$ are also approximated with a normal function:

$$\frac{\overline{U} - \overline{U}_\infty}{\overline{U}_{CL} - \overline{U}_\infty} = \exp\left[-\ln(2)\left(\frac{\zeta}{\zeta_{0.5}}\right)^2\right] \tag{8}$$

where $\zeta_{0.5} = r_{0.5}/(x - x_0)$ is the radial expansion rate derived from Fig. 7. Eq. (8) is plotted in Fig. 8 as a solid line and it matches reasonably well with the experimental data. The self-similar feature of the normalized velocities becomes evident after $x/D = 15$, and is also qualitatively comparable to those of a clean gaseous jet (Hussein et al., 1994). This suggests that the underlying flow field of the spray jets investigated is very close to a conventional jet flow, and its turbulence structure should be able to be computed with accuracy by the existing CFD codes for further evaluation of the droplet dispersion and evaporation submodels.

Self-similar velocity distributions as described by Eq. (8) are also found for droplets conditioned on different size classes. However, the value of the virtual origin, x_0, in defining ζ decreases with droplet size as is evident in Fig. 7, and must be distinguished from that obtained from Eq. (7) for describing the decay of the centreline axial velocity in Fig. 6. The latter is linked to the initial acceleration of large droplets as discussed earlier.

The normalized profiles of both $(\overline{U}_0 - \overline{U}_\infty)/(\overline{U}_{CL} - \overline{U}_\infty)$, and $u'_{CL}/\overline{U}_0$ conditioned on droplets smaller than 3 μm are plotted in Fig. 9 for the three high-speed spray jets investigated. Size discrimination is used to approximate to the gas velocity. No clear difference is observed in either $(\overline{U}_0 - \overline{U}_\infty)/(\overline{U}_{CL} - \overline{U}_\infty)$ or

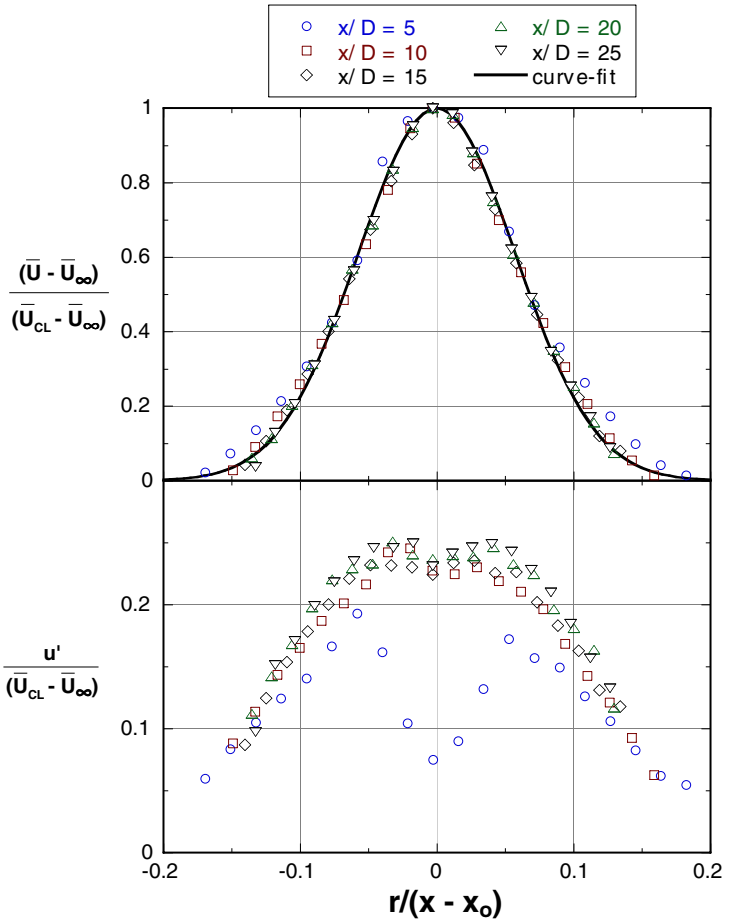

Fig. 8. Normalized axial mean, $(\overline{U}-\overline{U}_\infty)/(\overline{U}_{CL}-\overline{U}_\infty)$, and rms, $u'/(\overline{U}_{CL}-\overline{U}_\infty)$, velocities of droplets conditioned on $d<3$ μm for spray jet LFS. The solid line is a curve-fit using Eq. (8).

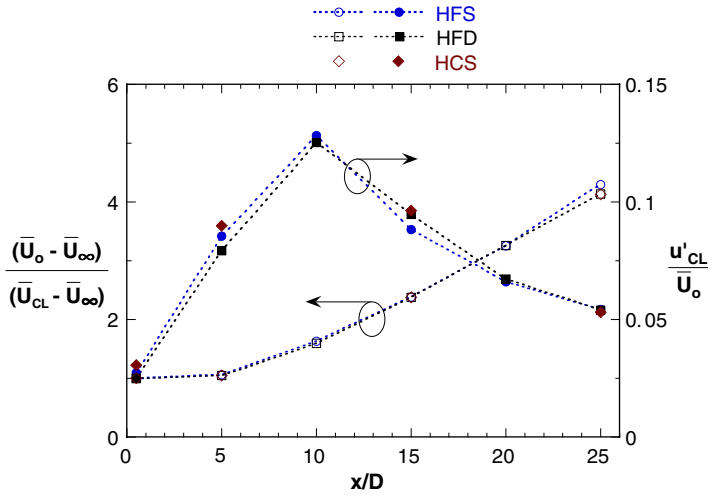

Fig. 9. Variation of the reciprocal of the normalized centreline axial mean velocity, $(\overline{U}_0-\overline{U}_\infty)/(\overline{U}_{CL}-\overline{U}_\infty)$, and the normalized centreline axial rms velocity, $u'_{CL}/\overline{U}_0$, of droplets conditioned on $d<3$ μm for the three high-speed spray jets investigated.

$u'_{CL}/\overline{U}_0$, despite the fact that the droplet mass loading of HFD is almost twice that of HFS at the nozzle exit. In fact, the normalized droplet mean and rms velocities conditioned on the other size classes also have the same values among the high-speed spray jets investigated here. This suggests that effects of flow modification may be neglected in the spray jets investigated, probably due to the low droplet mass loading at less than 2% and the small droplet Reynolds number (Hetsroni, 1989), $Re_d \equiv |U_s|d/\nu_g$, typically less than 10. A lack of flow modification is also consistent with the self-preserving flow field observed at downstream locations in Fig. 8. The decay rate of $(\overline{U}_{CL} - \overline{U}_\infty)/(\overline{U}_0 - \overline{U}_\infty)$, however, is slightly higher than that for the spray jet LFS shown in Fig. 6, but still lower than that of a clean gaseous jet (Hussein et al., 1994).

3.3. Droplet dispersion

Although a self-similar behaviour is found for the droplet mean and rms velocities at downstream axial locations, droplet motion can be quite different in the axial and radial directions and depends strongly on the droplet size. Also, the influence of initial conditions is important near the nozzle exit. Fig. 5 shows that large droplets with substantial inertia are still lagging behind the gas flow at $x/D = 5$ and thus remain accelerated in the potential core. At large radius, however, the trend is reversed with large droplets moving faster as the air flow velocity decreases drastically. Further downstream for $x/D > 5$, a positive axial mean slip velocity, $\overline{U}_s$, quickly develops for droplets of all size classes as the spray jet diverges. The centreline value of $\overline{U}_s$ is plotted in Fig. 10 for spray jet LFS versus the average droplet diameter, $\bar{d}$, of a particular size class. The almost linear relationship of $\overline{U}_s$ with increasing droplet size suggest that the Stokes drag force dominates the droplet motion in the axial direction.

The magnitude of $\overline{U}_s$ also reduces to zero with increasing radius at all the axial locations as can be inferred from Fig. 5. This feature is unlike the atomized non-evaporative (Karl et al., 1996; de Vega et al., 2000) or evaporative (McDonell and Samuelsen, 1995) sprays at downstream stations where the axial mean slip velocity remains finite on the spray edge for large droplets. The difference is related to the initial droplet size distributions across the sprays. For air-assisted liquid jet atomization with or without swirl (Lasheras et al., 1998), most large droplets formed after the primary break-up stay on the spray edge where the secondary break-up, via turbulent motion of the carrier fluid, is less effective than near the centreline. By contrast, the probability of finding big droplets near the nozzle edge on the exit plane is relatively low for the present two-phase jet flows as seen in Fig. 4.

Moreover, the radial mean drag force is almost negligible here since there is no initial radial momentum applied to the droplets. Indeed, no clear dependency of the radial mean velocity on droplet size has been observed such that larger droplets with substantial inertia do not travel comparatively faster to accumulate on the spray edge, in contrast to the atomized sprays (McDonell and Samuelsen, 1995; de Vega et al.,

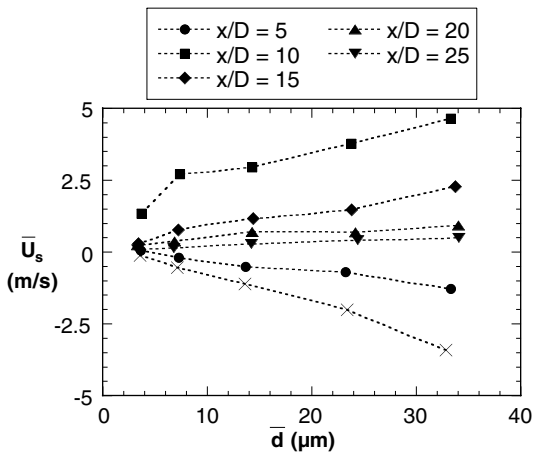

Fig. 10. Centreline axial mean slip velocity, $\overline{U}_s$, of the spray jet LFS plotted against the average diameter of droplets, $\bar{d}$, conditioned on different size classes at $x/D = 0.5$: ×; $x/D = 5$: ●; $x/D = 10$: ■; $x/D = 15$: ♦; $x/D = 20$: ▲; and $x/D = 25$: ▼.

2000). These arguments further indicates the importance of the initial conditions on the development of downstream structure of the spray jet flows in general. The lack of significant radial mean slip velocity between droplets of different size classes, however, does not apply to the instantaneous drop motion, as discussed below.

The development of downstream droplet rms velocities conditioned on different size classes is quite different from the mean velocity field, and can be better illustrated by the scatter plots of instantaneous droplet axial, U, and radial, V, velocities versus droplet diameter, d. Fig. 11 shows such typical plots near the jet centreline at $x/D = 15$ for spray jet HFS. The scattering of the V velocity component reduces consistently with increasing values of d, implying a weakening response to turbulent fluctuations of the carrier flow. This inertia effect is reflected by the drastic increase of the local Stokes number, St, as shown by the solid line in Fig. 11. St for a droplet of diameter d is defined as the droplet relaxation time, $t_d = \rho_\ell d^2/18\rho_g \nu_g$, over the Kolmogorov time scale, $t_\eta \equiv (\nu_g/\epsilon)^{0.5}$:

$$St \equiv \frac{t_d}{t_\eta} = \left(\frac{\rho_\ell}{\rho_g}\right)\frac{Re^{3/2}}{18}\left(\frac{d}{\ell}\right)^2 \tag{9}$$

Here $Re \equiv u'_g \ell/\nu_g$ is the turbulence Reynolds number with ν the kinematic viscosity. The turbulence kinetic energy dissipation, ϵ, is estimated as u'^3_g/ℓ with u'_g the local axial rms velocity conditioned on droplets less than 3 μm. The longitudinal integral length scale, ℓ, is taken as $0.65r_{0.5}$ (Antonia and Bilger, 1973) with $r_{0.5}$ the half-radius of the axial mean velocity excess, also conditioned on droplets less than 3 μm. A uniform distribution of ℓ across the jet is assumed here at downstream locations with sufficient accuracy (Chen et al., 1996).

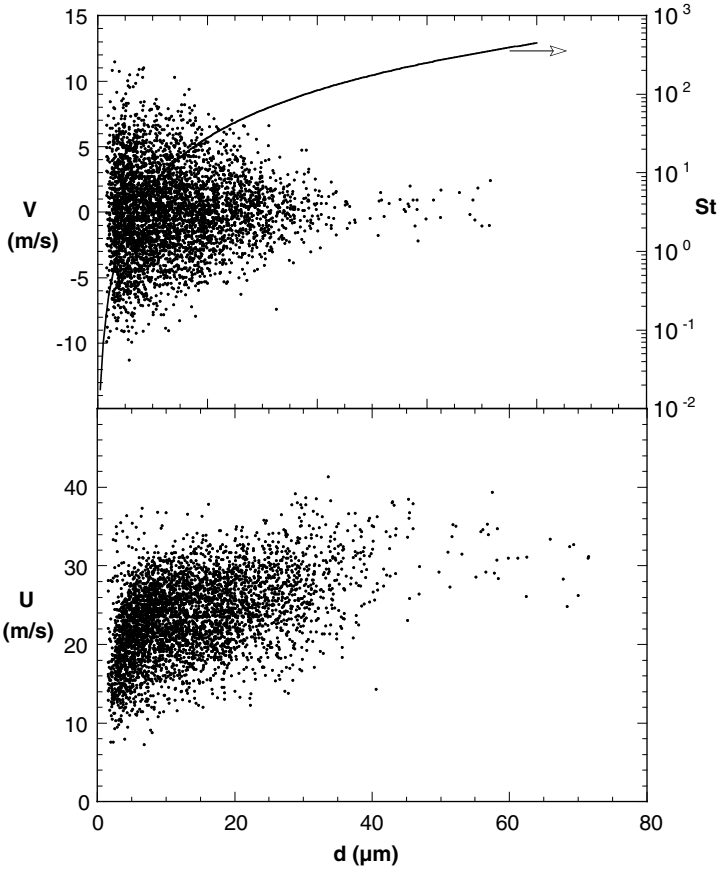

Fig. 11. Scatter plots of the instantaneous droplet axial, U, and radial, V velocity versus droplet diameter, d, near the jet centreline at $x/D = 15$ for spray jet HFS. The dependency of Stokes number on droplet diameter calculated via Eq. (9) is also shown in a line.

Eq. (9) implies that the smaller the local Stokes number for droplets of a particular diameter, the more readily they can follow turbulent fluctuations of the carrier flow. Based on this argument, values of both u' and v' at $x/D = 5$ become highest for small droplets conditioned on $d < 5$ μm and lowest for droplets conditioned in the size class of 30 μm $< d <$ 40 μm in Fig. 5. Also, the maximum difference of u' and v' between small and large droplets is found in the mixing layer between $r/D = 0.4$ and 0.6, where intense turbulent mixing takes place.

Further downstream of $x/D > 5$, the differences between the values of v' conditioned on different size classes remain finite due to the same inertia effect and a wide range of the droplet Stokes number. This is demonstrated in Fig. 12 where the absolute magnitude of v' conditioned on a particular droplet size class relative to that conditioned on droplets less than 3 μm, $v'/v'|_{d<3\ \mu m}$, decreases consistently with $\overline{St}$ for $x/D > 5$. Here, $\overline{St}$ is the averaged droplet Stokes number of a particular size class given as

$$\overline{St} = \frac{\bar{t}_d}{t_\eta} \tag{10}$$

with the equivalent droplet relaxation time $\bar{t}_d = \rho_\ell \overline{d^2}/18\rho_g \nu_g$. Note the use of the Kolmogorov time scale t_η as the characteristic flow time in defining the Stokes number in Eq. (10) gives a better correlation with $v'/v'|_{d<3\,\mu m}$ than either the integral time scale, ℓ/u'_g, or the flow residence time, $\ell/\overline{U}|_{d<3\,\mu m}$.

Fig. 12 also implies that the radial motion of droplets in the present spray jets is mainly subject to local turbulent fluctuations of the carrier flow. For spray jet LFS, the estimated Kolmogorov length scale, $\eta = \ell/Re^{3/4}$, is smallest at $x/D = 5$, and is 33 μm on the axis and 20 μm in the mixing layer. Since the maximum droplet size of 40 μm in Fig. 12 is smaller than most of the turbulence length scales in the flow field, the response of droplet radial motion to turbulent fluctuations would certainly be reduced with increasing values of $\bar{t}_d$ when the droplets are trapped by these turbulence structures. The deviation of v' from that of the carrier flow represented by v' conditioned on droplets smaller than 3 μm, $v'|_{d<3\,\mu m}$, starts approximately at $\overline{St} = 1$.

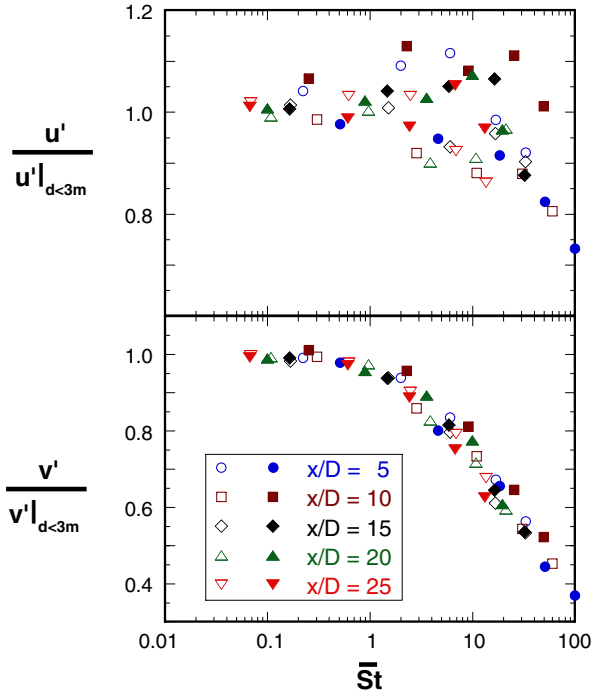

Fig. 12. Relative droplet axial, $u'/u'|_{d<3\,\mu m}$, and radial, $v'/v'|_{d<3\,\mu m}$, rms velocity versus the averaged droplet Stokes number of a particular size class along the jet centreline (open symbols) as well as at the half-radius of the axial mean velocity profile (solid symbols) for spray jet LFS at $x/D = 5$: ○ and ●; $x/D = 10$: □ and ■; $x/D = 15$: ◇ and ◆; $x/D = 20$: △ and ▲; and $x/D = 25$: ▽ and ▼.

Unlike v', the droplet axial rms velocities, u', conditioned on different size-classes come quickly to almost the same value for $x/D > 10$ as shown in Fig. 5, and thus do not exhibit a strong dependency on $\overline{St}$ as seen in Fig. 12. This feature does not derive from the initial condition and has been ascribed before to the "overshooting" effect (Hinze, 1972) or the "fan spreading" phenomenon (Hardalupas et al., 1989) in non-homogeneous turbulent flows. Its cause lies mainly in the migration of droplets with substantial inertia between regions of different axial mean velocities. Along with the divergence of the spray jets, droplets are dispersed radially into neighbouring regions. The ability of droplet cross-stream dispersion can be characterized by the velocity ratio of $v'/\overline{U}$ for a particular size class. But, as discussed before, the velocity of large droplets with $\overline{St} > 1$ does not respond immediately to the changing flow environment. As these large droplets are dispersed into a region of a different axial mean velocity, they still retain, to varying degrees, their previous values of the instantaneous axial velocity, U. This lack of an immediate response in the droplet velocity broadens the scattering of the U-component such that u' does not follow the similar relationship for v' as shown in Fig. 12, e.g. u' does not decrease consistently with increasing $\overline{St}$. This "memory" effect induces the broadening of the U-component scattering and is described by the ratio of the equivalent droplet relaxation time, $\bar{t}_d$, over the time scale, t_m, for the rate of the incremental change of $\overline{U}$ in the radial direction experienced by the droplets. The characteristic time scale t_m may be estimated as

$$t_m \approx \left[\frac{v'}{\overline{U}}\left|\frac{\partial \overline{U}}{\partial r}\right|\right]^{-1} \sim \frac{r_{0.5}}{v'} \tag{11}$$

The order-of-magnitude approximation in Eq. (11) suggests that t_m scales with the "genuine" droplet Lagrangian integral time scale that is not biased by the "memory" effect.

The above arguments highlight the dominating influence of the droplet axial mean velocity gradient on the magnitude of the droplet axial rms velocity for spray jet flows in general. This behaviour is in contrast to the strong dependency of the droplet radial rms velocity on the droplet response to turbulent fluctuations of the carrier flow as discussed before. One particular consequence of the different underlying mechanisms between the droplet axial and radial fluctuation velocities is their increasing anisotropy with the time scale ratio of $\bar{t}_d/t_m$ at downstream axial stations, as demonstrated in Fig. 13. The droplet centreline rms velocity ratio, u'_{CL}/v'_{CL}, relative to that conditioned on droplets smaller than 3 μm $(u'_{CL}/v'_{CL})|_{d<3\,\mu m}$, increases drastically when $\bar{t}_d/t_m$ exceeds approximately 0.3 at $x/D = 20$ and 25 for both high-speed and low-speed spray jets. The departure of $(u'_{CL}/v'_{CL})/(u'_{CL}/v'_{CL})|_{d<3\,\mu m}$ from unity is attributed to the decrease of v', but not u', with an increasing equivalent droplet relaxation time $\bar{t}_d$.

3.4. Mean droplet diameter and number density distribution

Statistics of the droplet size is given by the radial profiles of the Sauter mean diameter (SMD), d_{32}, in Fig. 14. SMD is the diameter of a hypothetical drop having the same volume/surface ratio as the full drop

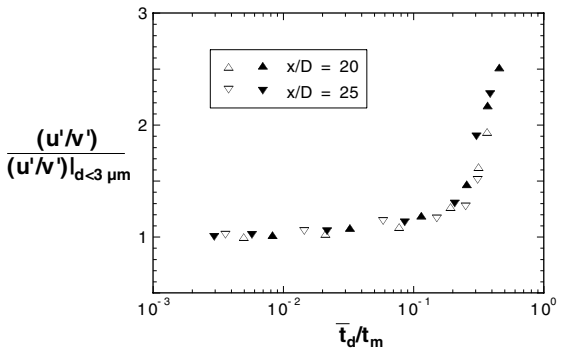

Fig. 13. Relative centreline rms velocity ratio, $(u'_{CL}/v'_{CL})/(u'_{CL}/v'_{CL})|_{d<3\,\mu m}$, versus the time scale ratio of $\bar{t}_d/t_m$ for spray jets LFS (open symbols) and HFS (solid symbols) at downstream axial locations.

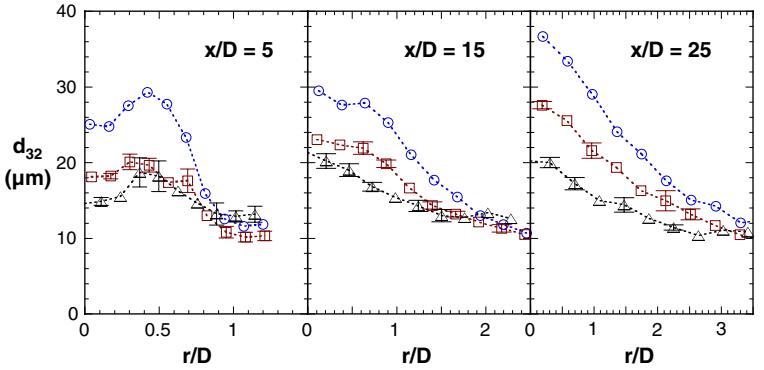

Fig. 14. Radial profiles of the Sauter mean diameter, d_{32}, for spray jet HFS: □; HCS: ○; LFS: △. The error bars show the range of variation due to data asymmetry on both sides of the centreline.

distribution. It expresses a measure of droplet fineness in terms of the total surface area, and thus is more relevant for characterizing evaporative sprays than the other mean diameters. On the jet axis, d_{32} increases monotonically with the normalized axial distance, x/D, up to $x/D = 25$ for all the high-speed spray jets. The increase of the centreline value of d_{32} is related to the faster decline of the number of small droplets than that of large droplets, as d_{10} increases as well. It is partly because that more small droplets are transported away from the axis than large ones, and partly due to a shorter life time, t_e, for smaller droplets with t_e expressed as (e.g. Bird et al., 1960, Chapter 21).

$$t_e = \left(\frac{\rho_\ell}{\rho_g}\right)\frac{d^2}{4\mathscr{D}\ln(1+B)Sh} \tag{12}$$

for a droplet of diameter d. Here $\mathscr{D}$ is the diffusivity of acetone vapour in air, $B = (X_{ac,s} - \overline{X}_{ac})/(1 - X_{ac,s})$ is the transfer number, and Sh is the Sherwood number, which may be estimated from the following empirical formula for convective mass transfer:

$$Sh = 2 + 0.6Re_d^{1/2}Sc^{1/3} \tag{13}$$

with the Schmidt number, $Sc \equiv \nu_g/\mathscr{D}$.

Further downstream, the mean diameter d_{32} must eventually decrease mainly because of the depletion of large droplets via evaporation. This occurs already for spray jet LFS at $x/D > 15$ as indicated by the evolution of the probability density function, $p(d)$, for droplet diameter along the axis in Fig. 15. The percentage of droplets greater than 6 μm increases from the nozzle exit plane up to $x/D = 10$ for the low-speed spray jet LFS and then drops quickly for $x/D > 15$. Such feature is not observed in the high-speed spray jets up to $x/D = 25$, presumably due to the relatively shorter droplet travel time at a higher axial mean velocity, $\overline{U}_{CL}$. The droplet travel time, or its flight time, can be derived by integration of the reciprocal of $\overline{U}_{CL}$ along the axis, and is 8.5 ms for spray jet LFS at $x/D = 15$. The axial location corresponding to the same order of flight time is approximately $x/D = 25$ in the high-speed spray jets. The life time, t_e, of a 10-μm droplet released on the exit plane in spray jet LFS is also found to be around 8.5 ms by using Eqs. (12) and (13). The time t_e given by Eq. (12) is only an order-of-magnitude estimate since the effects of turbulence on droplet evaporation are not included.

A monotonic decrease of d_{32} with the radial distance is observed in Fig. 14 at all the axial locations except $x/D = 5$ (where d_{32} peaks around $r/D = 0.4$, as do the other mean droplet diameters, e.g. d_{10}). This location coincides with the mixing layer of intense turbulence as seen in Fig. 5. Higher turbulence is believed to enhance the droplet evaporation rate, and thus depletes locally more small droplets. This effect is further illustrated in Fig. 16 which shows the radial profiles of $N_c/N_{CL,c}$, the normalized number density conditioned in the size class of $10\ \mu m < d < 20\ \mu m$ and $d < 5\ \mu m$ at several axial locations. The unconditional number density normalized by the centreline value, N/N_{CL}, is also shown for comparison. The local minimum of $N_c/N_{CL,c}$

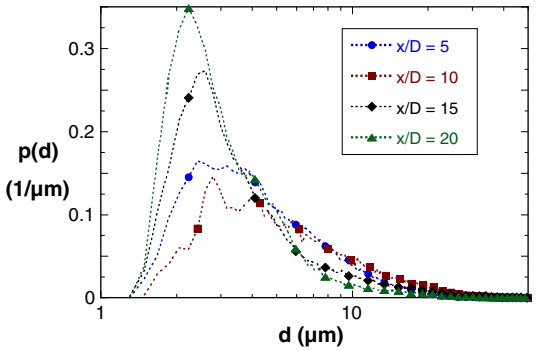

Fig. 15. Evolution of the probability density, $p(d)$, of droplet diameter along the centreline of the spray jets LFS. The droplet diameter, d, is plotted in log scale.

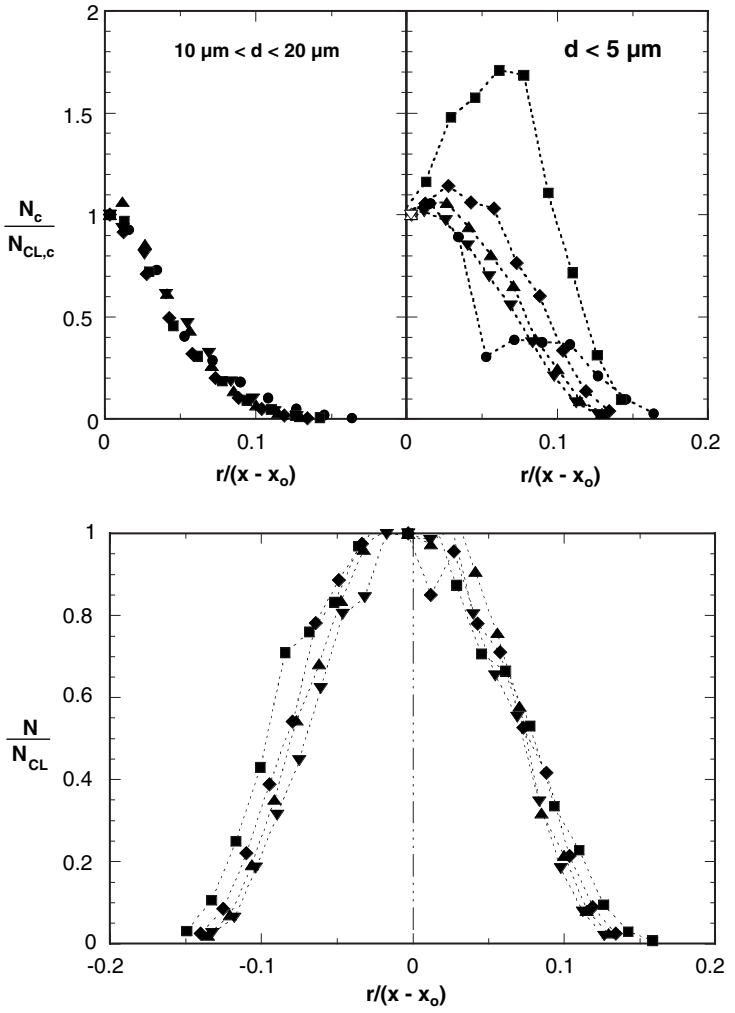

Fig. 16. Radial profiles of the normalized number density, N/N_{CL}, and that conditioned on a particular size class, $N_c/N_{CL,c}$, for spray jet LFS at $x/D = 5$: ●; $x/D = 10$: ■; $x/D = 15$: ♦; $x/D = 20$: ▲; and $x/D = 25$: ▼.

conditioned on $d < 5$ μm at $x/D = 5$ indicates a sudden decline in the number of small droplets at this radial position. Such feature is not observed in the radial profile of $N_c/N_{CL,c}$ conditioned on 10 μm $< d <$ 20 μm.

Evaporation of small droplets is more effectively enhanced by turbulence as they can better "sense" the presence of intense turbulence at the mixing layer. Large droplets, on the other hand, evaporate mainly via a high slip velocity relative to the carrier flow as described by an empirical formula similar to Eq. (13). In fact, a self-similar distribution for the radial profiles of $N_c/N_{CL,c}$ conditioned on 10 μm $< d <$ 20 μm can be inferred at downstream axial locations in Fig. 16. The local maximum of $N_c/N_{CL,c}$ conditioned on $d < 5$ μm at $x/D = 10$ is attributed to the dispersion effect in line with the increase of d_{32} along the axis mentioned before.

The magnitude of d_{32} is found almost the same for spray jets HFS and HFD at all the measuring locations. The initial conditions as seen in Table 1 are quite similar for both spray jets, except that the drop mass loading of HFD is approximately twice as much as that of HFS at the jet exit. This behaviour implies that the droplet mass loading has little influence on the mean diameters and hence the evaporation rate of individual droplets, given that the mean acetone vapour mole fraction, $\overline{X}_{ac}$, is far from the saturation value, $X_{ac,s}$, and that effects of droplet-droplet interactions, e.g. coalescence, are expected to be negligible for these dilute sprays.

3.5. Evaporation rates of spray jets

Radial profiles of the local acetone droplet and vapour mass fluxes, $\dot{m}_d$ and $\dot{m}_g$, are shown in Fig. 17 for spray jets HFS and LFS at several axial locations from $x/D = 5$ to 20. In general, both $\dot{m}_d$ and $\dot{m}_g$ peak on the jet axis and decrease with an increasing axial distance. A larger radial dispersion of the gas phase than that of the droplets is also evident at downstream locations. This radial spreading is stronger for the low-speed spray jet LFS than the high-speed one, HFS. At a particular axial location, higher droplet mass flux is found for HFS, mainly due to its higher mass loading at the nozzle exit.

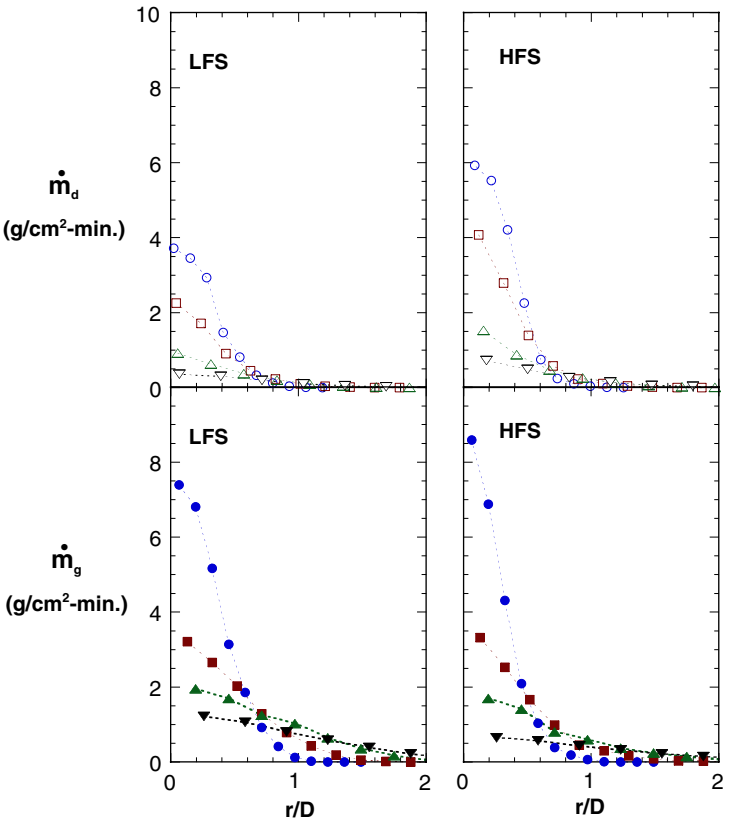

Fig. 17. Radial profiles of mass flux of acetone droplets, $\dot{m}_d$, (open symbols) and vapour, $\dot{m}_g$, (closed symbols) for spray jets HFS and LFS at $x/D = 5$: ○ and ●; $x/D = 10$: □ and ■; $x/D = 15$: △ and ▲; and $x/D = 20$: ▽ and ▼.

A measure of the bulk evaporation rate can be obtained from Fig. 17 by integration of $\dot{m}_d$ across the jet at all axial locations. The axial variation of these integrated droplet fluxes, $\dot{m}_{I,d}$, is plotted in Fig. 18. It is clear that the values of $\dot{m}_{I,d}$ measured near the nozzle exit must be in error for the highspeed spray jets (shown in dashed lines), as they must decrease with increasing x/D due to evaporation. The recorded nozzle droplet flux is most in error for the dense spray jet HFD, which should have the highest number density near the nozzle exit. The cause of this error is that the droplet number density is so high ($>10^5/cm^3$) such that multiple droplets may co-exist in the probe volume. The probe size of 110 μm corresponds to approximately 6 pixels in Fig. 2(b), within which overlap of droplet signatures is clearly visible. Such events cannot be recorded as valid data points by the PDI instrument and thus lead to a reduced number density in the measurements. This reduction is confirmed in Fig. 19 where the sum of the integrated vapour and droplet fluxes, $\dot{m}_{I,g}$ and $\dot{m}_{I,d}$, both normalized by the fuel injection rate, $\dot{G}$, is less than unity for $x/D < 10$. Based on mass conservation, this sum is the total flux, which should be a conserved scalar. An uncertainty of 10% for the measurements of $\dot{m}_{I,d}$ at downstream axial locations can also be inferred from Fig. 19, and is shown in the error bars for the low-speed spray jet LFS in Fig. 18.

The mass flux of droplets integrated on a particular plane normal to the axial axis, $\dot{m}_{I,d}$, is related to the local ensemble-averaged mean droplet evaporation rate, $\bar{\dot{m}}$, as

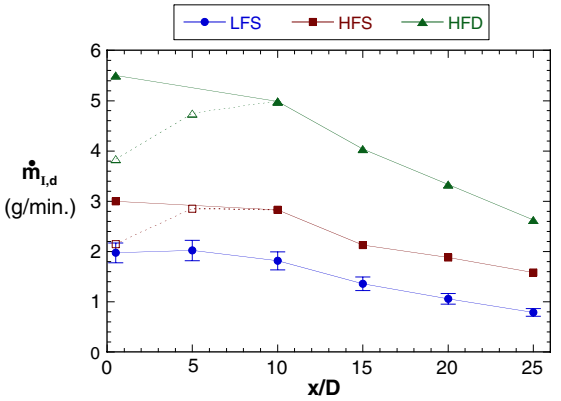

Fig. 18. Longitudinal evolution of the droplet mass flux integrated across the jet, $\dot{m}_{I,d}$, for spray jets LFS: ●; HFS: ■; and HFD: ▲. The error bars show 10% measurements uncertainty. The unfilled symbols connected by dashed lines indicate erroneous measurements.

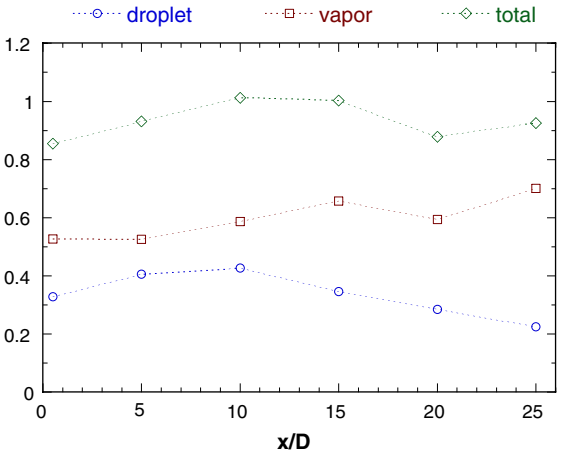

Fig. 19. Longitudinal evolution of the measured acetone mass flux, integrated across the jet and normalized by the injection rate, $\dot{G}$, for spray jet HFD. ○: $\dot{m}_{I,d}/\dot{G}$; □: $\dot{m}_{I,g}/\dot{G}$; ◇: $(\dot{m}_{I,d} + \dot{m}_{I,g})/\dot{G}$.

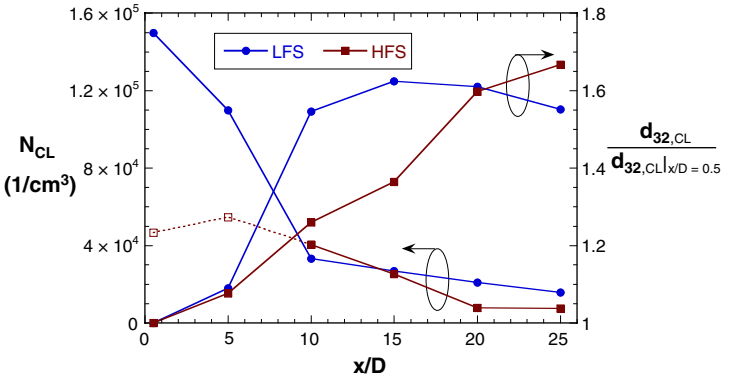

Fig. 20. Comparison of the centreline number density, N_{CL}, and the centreline SMD, $d_{32,CL}$, normalized by that at $x/D = 0.5$, $d_{32,CL}|_{x/D=0.5}$ along the axis for the spray jets LFS and HFS. The unfilled symbols connected by dashed lines indicate erroneous measurements.

$$\frac{d\dot{m}_{I,d}}{dx} = \int_0^{+\infty} 2\pi r N \bar{\dot{m}}\, dr \tag{14}$$

based on the conservation of drop mass evaporated. The left-hand side of Eq. (14) can be obtained from reading the slope of $\dot{m}_{I,d}$ in Fig. 18, which characterizes the bulk evaporation rate of the spray jets. The general trend shows that the bulk evaporation rate is higher in far-field than near-field (within 10 nozzle diameters from the exit plane) for all the spray jets investigated. This difference is attributed to a much lower $\bar{\dot{m}}$ in near-field than far-field on the right-hand side of Eq. (14). The bulk evaporation rate appears to be highest at an axial location between $x/D = 10$ and 15, where the axial mean slip velocity reaches approximately its maximum along the centreline. It is also readily seen that the bulk evaporation rate is higher in a dense (HFD) than sparse (HFS) spray due mainly to the higher droplet number density, N, on the right-hand side of Eq. (14). The averaged droplet evaporation rate, $\bar{\dot{m}}$, may not differ too much as the flow field is quite similar for spray jets HFD and HFS.

On the other hand, the longitudinal evolution of $\dot{m}_{I,d}$ shows almost the same decreasing rate at $x/D > 15$ for spray jets HFS and LFS in Fig. 18. Although the bulk evaporation rate is comparable at these downstream axial locations, the droplet evaporation rate, $\bar{\dot{m}}$, on the right-hand side of Eq. (14) is not the same for spray jets HFS and LFS. As indicated in Fig. 20, the centreline value of the droplet number density, N_{CL}, is much less in the highs-peed spray HFS than in the low-speed spray LFS at $x/D > 15$. In view of the self-similarity of N/N_{CL} suggested in Fig. 16, the droplet number density, N, must be lower in HFS than in LFS everywhere across the radial profile at the same downstream axial location. As such, the averaged droplet evaporation rate, $\bar{\dot{m}}$, must be higher in HFS than in LFS. This is attributed to the combined effects of higher turbulence and higher mean slip velocities in the spray jet HFS.

4. Conclusions

This paper presents an experimental study of droplet dispersion and evaporation in turbulent non-reacting dilute spray jets. The simplicity of the flow configuration and well-defined boundary and initial conditions should enable CFD specialists to apply the results with confidence for comparison with simulations based on a variety of numerical schemes. Detailed measurements of spray properties have been reported for four spray jets of different loadings and flow conditions with the tabulated data available upon request. The choice of a highly volatile liquid, i.e. acetone, makes these data sets especially useful for testing the evaporation submodels. Major findings on the spray jet structure are summarized as follows:

(1) Flow modulation effects are found to be negligible in the spray jets investigated, and the underlying flow field of the carrier gas is very similar to that of a conventional jet. Droplet motion is subject mainly to the drag force exerted by the carrier gas flow. Hence, the size-classified axial mean slip velocity along the

centreline scales almost linearly with the average droplet diameter conditioned in a particular size class. There is however no mean slip velocity developed in the radial direction as no radial mean drag force exists at the nozzle exit.

(2) Self-similar distributions are observed at downstream locations of $x/D > 15$ for the radial profiles of size-classified droplet mean and rms velocities as well as of the droplet number density conditional on a size class of relatively large diameter. The virtual origin derived from the normalized axial mean velocity profile increases with the droplet size, whereas the spray expansion rate decreases. Both trends indicate that the decay of the axial mean velocity along the jet direction is retarded for large droplets with significant inertia. The virtual origin for describing the size-classified self-similar velocity distributions, on the other hand, decreases with the droplet size.

(3) Substantial droplet dispersion effects are observed and are reflected in the different behaviours of the axial and radial components of the size-classified droplet rms velocity. The droplet radial rms velocity decreases consistently with the Stokes number when it is greater than a threshold value. A unity threshold value occurs when the Kolmogorov time scale is used as the characteristic flow time in the definition of the Stokes number. The droplet axial rms velocity may increase with the Stokes number as a result of droplets migration in the radial direction between regions of different axial mean velocities. This ''overshooting'' effect is better characterized by the time scale ratio of the droplet relaxation time over a time scale equivalent to the ''genuine'' droplet Lagrangian integral time scale.

(4) Turbulence-enhanced droplet evaporation is observed at the mixing layer of $x/D = 5$ for the spray jets investigated here and has a marked effect in removing droplets smaller than 5 μm in size, which can follow the instantaneous flow motion. The bulk evaporation rate is found comparable at downstream locations for a high-speed and a low-speed spray jet of the same liquid acetone injection rate, and it increases with the injection rate. The local ensemble-averaged mean droplet evaporation rate, on the other hand, is much higher in the high-speed than in the low-speed spray jet due to the combined effects of high turbulence and high mean slip velocity.

Acknowledgement

This work is supported by the Australian Research Council.

References

Antonia, R.A., Bilger, R.W., 1973. An experimental investigation of an axisymmetric jet in a co-flowing air stream. J. Fluid Mech. 61, 805–822.

Antonia, R.A., Prabhu, A., Stephenson, S.E., 1975. Conditionally sampled measurements in a heated turbulent jet. J. Fluid Mech. 72, 455–480.

Balachandar, R., 1998. A note on the characteristics of droplet-laden jets. ASME J. Fluids Eng. 120, 403–406.

Bazile, R., Stepowski, D., 1995. Measurements of vaporized and liquid fuel concentration fields in a burning spray jet of acetone using planar laser induced fluorescence. Exp. Fluids 20, 1–9.

Bellan, J., 2000. Supercritical (and subcritical) fluid behavior and modeling: drops, streams, shear and mixing layers, jets and sprays. Prog. Eng. Comb. Sci. 26, 329–366.

Berlemont, A., Grancher, M.S., Gouesbet, G., 1995. Heat and mass transfer coupling between vaporizing droplets and turbulence using a Lagrangian approach. Int. J. Heat Mass Transfer 38, 3023–3034.

Bilger, R.W., 1992. Advanced laser diagnostics: implications of recent results for advanced combustor models. In: Lee, R., Whitelaw, J., Wung, T. (Eds.), Aerothermodynamics in Combustors. Springer-Verlag, Heidelberg, pp. 3–16.

Bird, R.B., Stewart, W.E., Lightfoot, E.N., 1960. Transport Phenomena. John Wiley & Sons, New York.

Bryant, R.A., Donbar, J.M., Driscoll, J.F., 2000. Acetone laser induced fluorescence for low pressure/low temperature flow visualization. Exp. Fluids 28, 471–476.

Chen, Y.-C., Peters, N., Schneemann, G.A., Wruck, N., Renz, U., Mansour, M.S., 1996. The detailed flame structure of highly stretched turbulent premixed methane-air flames. Combust. Flame 107, 223–244.

Chen, Y.-C., Stårner, S.H., Masri, A.R., 2001. Combined PDA/LIF measurements in simple, evaporating turbulent spray jets. Proceedings of the 14th Australasian Fluid Mechanics Conference, 267–270.

Chen, Y.-C., Stårner, S.H., Masri, A.R., 2002. Characteristics of turbulent spray combustion in a piloted jet flame burner. Proc. Combust. Inst. 29, 532–625.

de Vega, M., Rodríguez, P., Lecuona, A., 2000. Mean structure and droplet behavior in a coaxial airblast atomized spray: self-similarity and velocity decay function. Atomiza. Sprays 10, 603–626.
Faeth, G.M., 1996. Spray combustion phenomena. Proc. Combust. Inst. 26, 1593–1612.
Fan, L.S., Lau, R., Zhu, C., Vuong, K., Warsito, W., Wang, X., Liu, G., 2001. Evaporative liquid jets in gas–liquid–solid flow system. Chem. Eng. Sci. 56, 5871–5891.
Ferrand, V., Bazile, R., Borée, J., 2001. Measurements of concentration per size class in a dense poly dispersed jet using planar laser-induced fluorescence and phase Doppler techniques. Exp. Fluids 31, 597–607.
Ferrand, V., Bazile, R., Borée, J., Charnay, G., 2003. Gas-droplet turbulent velocity correlations and two-phase interaction in an axisymmetric jet laden with partly responsive droplets. Int. J. Multiphase flow 29, 195–217.
Fleckhaus, D., Hishida, K., Maeda, M., 1987. Effect of laden solid particles on the turbulent flow structure of a round free jet. Exp. Fluids 5, 323–333.
Gouesbet, G., Berlemont, A., 1999. Eulerian and Lagrangian approaches for predicting the behaviour of discrete particles in turbulent flows. Prog. Eng. Comb. Sci. 25, 133–159.
Hardalupas, Y., Taylor, A.M.K.P., Whitelaw, J.H., 1989. Velocity and particle-flux characteristics of turbulent particle-laden jets. Proc. R. Soc. London A 426, 31–78.
Hetsroni, G., Sokolov, M., 1971. Distribution of mass, velocity, and intensity of turbulence in a two-phase turbulent jet. J. Appl. Mech. 93, 315–327.
Hetsroni, G., 1989. Particle–turbulence interaction. Int. J. Multiphase flow 15, 735–746.
Hinze, J.O., 1972. Turbulent and fluid particle interaction. Prog. Heat Mass Transfer 6, 433–452.
Hussein, H.J., Capp, S.P., George, W.K., 1994. Velocity measurements in a high-Reynolds-number, momentum-conserving, axisymmetric, turbulent jet. J. Fluid Mech. 258, 31–75.
Karl, J.-J., Huilier, D., Burnage, H., 1996. Mean behaviour of a coaxial air-blast atomized spray in a co-flowing air stream. Atomiza. Sprays 6, 409–433.
Kennedy, I.M., Moody, M.H., 1998. Particle dispersion in a turbulent round jet. Exp. Thermal Fluid Sci. 18, 11–26.
Lasheras, J.C., Villermaux, E., Hopfinger, E.J., 1998. Break-up and atomization of a round water jet by a high-speed annular air jet. J. Fluid Mech. 357, 351–379.
McDonell, V.G., Samuelsen, G.S., 1993. Structure of vaporizing pressure atomized sprays. Atomiza. Sprays 3, 321–364.
McDonell, V.G., Samuelsen, G.S., 1995. An experimental data base for the computational fluid dynamics of reacting and nonreacting methanol sprays. ASME J. Fluids Eng. 117, 145–153.
McDonell, V.G., Samuelsen, G.S., 1996. Intra- and inter-laboratory experiments to evaluate the performance of phase Doppler interferometry. In: Kuo, K. (Ed.), Recent Advances in Spray Combustion: Spray Atomization and Drop Burning Phenomena. American Institute of Aeronautics and Astronautics, VA, pp. 57–106.
McLaughlin, D.K., Tiederman, W.G., 1973. Biasing correction for individual realization of laser anemometer measurements in turbulent flows. Phys. Fluids 16, 2082–2088.
Modarress, D., Tan, H., Elghobasi, S., 1984. Two-component LDA measurement in a two-phase turbulent jet. AIAA J. 22, 624–630.
Mostafa, A.A., Mongia, H.C., McDonell, V.G., Samuelsen, G.S., 1989. Evolution of particle-laden jet flows: a theoretical and experimental study. AIAA J. 27, 167–183.
Nickels, T.B., Perry, A.E., 1996. An experimental and theoretical study of the turbulent coflowing jet. J. Fluid Mech. 309, 157–182.
Nijdam, J.J., Stårner, S.H., Langrish, T.A.G., 2004. An experimental investigation of droplet evaporation and coalescence in a simple jet flow. Exp. Fluids 37, 504–517.
Prevost, F., Borée, J., Nuglisch, H.J., Charnay, G., 1996. Measurements of fluid/particle correlated motion in the far field of an axisymmetric jet. Int. J. Multiphase flow 22, 685–701.
Sirignano, W.A., 1993. Fluid dynamics of sprays—1992 Freeman scholar lecture. ASME J. Fluids Eng. 115, 345–378.
Solomon, A.S.P., Shuen, J.S., Zhang, Q.F., Faeth, G.M., 1985. Measurements and predictions of the structure of evaporating sprays. ASME J. Heat Transfer 107, 679–686.
Sommerfeld, M., 1998. Analysis of isothermal and evaporating turbulent sprays by phase-Doppler anemometry and numerical calculations. Int. J. Heat Fluid Flow 19, 173–186.
Widmann, J.F., Presser, C., Leigh, S.D., 2001. Improving phase Doppler volume flux measurements in low data rate applications. Meas. Sci. Technol. 12, 1180–1190.
Widmann, J.F., Presser, C., 2002. A benchmark experimental database for multiphase combustion model input and validation. Combust. Flame 129, 47–86.
Ye, J., Richards, C.D., 1996. Droplet and vapor transport in a turbulent jet. Proc. Combust. Inst. 26, 1679–1685.
Zuev, Y.V., Lepeshinskii, I.A., Sovetov, V.A., 1986. Experimental and numerical investigation of a gas-droplet polydisperse turbulent jet. Fluid Dynamics 21, 730–735.